G. Giannetti, S. Selleri, G. G. Gentili, G. Garcia-Contreras, J. Córcoles and J. A. Ruiz-Cruz, "Advanced Modeling of Circular Waveguide-Based Devices With Smooth Profiles Using Transformation Optics and Hierarchical Model Reduction," in IEEE Journal of Microwaves, vol. 4, no. 4, pp. 675-689, Oct. 2024, doi: 10.1109/JMW.2024.3454563.

IEEE Journal of
Microwaves

MTT-S
MHz to THz Community

Received 9 July 2024; revised 2 September 2024; accepted 2 September 2024. Date of publication 7 October 2024;
date of current version 9 October 2024.

Digital Object Identifier 10.1109/JMW.2024.3454563

Advanced Modeling of Circular Waveguide-Based Devices With Smooth Profiles Using Transformation Optics and Hierarchical Model Reduction

GIACOMO GIANNETTI [1] **(Graduate Student Member, IEEE), STEFANO SELLERI** [1] **(Senior Member, IEEE), GIAN GUIDO GENTILI** [2]**, GINES GARCIA-CONTRERAS** [3]**, JUAN CÓRCOLES** [4] **(Senior Member, IEEE), AND JORGE A. RUIZ-CRUZ** [4] **(Senior Member, IEEE)**

(Regular Paper)

[1]Department of Information Engineering, University of Florence, 50139 Florence, Italy
[2]Dipartimento di Elettronica, Informazione e Bioingegneria, Politecnico di Milano, 20133 Milan, Italy
[3]Departamento de Tecnología electrónica y de las Comunicaciones, Escuela Politécnica Superior, Universidad Autónoma de Madrid, 28049 Madrid, Spain
[4]Information Processing and Telecommunications Center, Universidad Politécnica de Madrid, 28040 Madrid, Spain

CORRESPONDING AUTHOR: Giacomo Giannetti (e-mail: giacomo.giannetti@unifi.it).

The work of Gian Guido Gentili was supported by the European Union under the Italian National Recovery and Resilience Plan (PNRR) of NextGeneration EU, partnership on "Telecommunications of the Future" (PE00000001 - program "RESTART," Structural Project SRE). The work of Gines Garcia-Contreras, Juan Córcoles, and Jorge A. Ruiz-Cruz was supported by the Spanish Government under Grant PID2020-116968RB-C32 (DEWICOM) and Grant TED2021-130650B-C21 (ANT4CLIM) funded by MCIN/AEI/10.13039/501100011033 (Agencia Estatal de Investigación) and by EU (European Union) "NextGenerationEU"/PRTR.

ABSTRACT A powerful and accurate analysis method for the full-wave analysis of circular waveguide-based devices is introduced. The method uses transformation optics, hierarchical model reduction, and the finite element method. First, transformation optics is applied to map the original device in a cylinder filled with an anisotropic and inhomogeneous medium. Second, exploiting a hierarchical model reduction approach, the electric field is expanded in terms of the modes of the circular waveguide in the transverse plane, while the longitudinal dependence of the fields is tackled by a 1D finite element method. The BCs are fulfilled rigorously. The 3D integrals arising from the discretization of the vector electric field equation are separable, thus allowing for solving radial and longitudinal integrals once and for all, while the angular integrals are the only ones to be computed for each specific device geometry. The limitations of the method are: (a) the input and output waveguides must be circular waveguides, even with different radii; (b) the device lateral surface must be expressed as a strictly-positive single-valued function in cylindrical coordinates; (c) the device profile must be smooth. The method is verified against full-wave simulations from commercial software and measurements available in the literature, showing good agreement and efficiency.

INDEX TERMS Circular waveguide, electromagnetic modeling, finite element method, modal analysis, model order reduction, transformation optics, waveguide analysis.

I. INTRODUCTION

Microwave waveguide devices exhibiting smooth tapers are common, for instance, in high-power microwave [1] and 3D-printed devices [2]. In the former case, smooth transitions avoid field concentration at sharp edges, thus increasing transmittable power before breakdown. Such structures are used in particle accelerators [3] and plasma heating [1]. In the latter case, smooth transitions are requested for structural reasons, since 3D-printed objects suffer from sharp edges due to mechanical and thermal stresses occurring during production [4].

To analyze structures with smooth tapers, the following traditional methods are available. In [5], a differential method is compared to mode matching (MM). There the transverse problem is solved and analyzed separately from the longitudinal problem. The resulting ABCD matrices are cascaded. However, the field maps at each longitudinal cross-section are needed and doubts arise about the fulfillment of the boundary conditions (BCs) for the magnetic field. In [6], a circular taper is analyzed using a stepwise discretization of the profile solved using MM, thus introducing an approximation of the profile. In any case, the most common and accurate method for solving tapers is the coupled mode (CM) method [7], [8], which is used to design tapers [9], [10].

For completeness, the analysis methods for devices with discrete steps are MM [11], integral equations [12], [13], boundary-integral resonant mode expansion (BI-RME) [11], [14], or finite element method (FEM) [15]. Commercial solvers such as the Fest3D package in CST [16] prefer integral equations and BI-RME since full segmentation techniques such as FEM are computationally expensive. For structures with $E-$ and $H-$plane symmetries, specific FEM formulations [17] speed up the calculations.

A recent method to analyze waveguide devices with smooth tapers is described in [18]. This method uses hierarchical model (HM) reduction, transformation optics (TO), and FEM. However, only tapers with a rectangular cross-section are considered there, thus limiting its fields of application. Next, HM and TO are briefly described.

HM reduction is a method developed to analyze structures featuring a preferred direction of propagation. A 3D problem is then split into two problems with reduced dimensions: a 1D problem along the direction of propagation and a 2D problem on the transverse plane. HM is applied first to electromagnetic problems in [18].

The TO or transformation electromagnetics [19], [20], [21] is applied to obtain a simplified yet equivalent problem. To date, research on TO has mostly focused on open problems, while closed problems have not been explored in depth. The latter requires a careful treatment of the BCs. In [22], transformation electromagnetics is applied to analyze arbitrarily shaped resonators, while in [23] it is used to treat rough surfaces. In [24], a numerical method for calculating eigenvalues is developed using a TO approach. In [25], the method introduced in [24] is corrected to properly enforce the BCs for the magnetic field in the TE modes. In [26], the MM technique is applied for the evaluation of the generalized scattering matrix (GSM) and the design of microwave components such as polarizers [27], [28] and filters.

This work extends the HM introduced in [18] to devices with smooth profiles based on circular waveguides (CWs). Since the HM in [18] is specifically formulated for rectangular waveguide devices, its application to CW devices is far from straightforward. Therefore, the method proposed here is original, since the peculiar transformation it uses, combined with the expansion in terms of Lagrange polynomials of the entries of the material parameters, reduces the 3D integrals into three classes of 1D integrals, all frequency independent, of which only one must be computed for each specific geometry, the others not depending on the geometry and thus can be pre-computed once and stored for usage in all the problems under study. In addition, the cross-section between the ports can be arbitrary, while it must be a rectangle in [18].

TABLE 1. List of Acronyms

Full name	Acronym
boundary condition	BC
boundary-integral resonant mode expansion	BI-RME
circular waveguide	CW
coupled mode	CM
degree of freedom	DOF
finite element method	FEM
generalized scattering matrix	GSM
hierarchical model	HM
mode matching	MM
original domain	OD
perfect electric conductor	PEC
perfect magnetic conductor	PMC
transformation optics	TO
transformed domain	TD

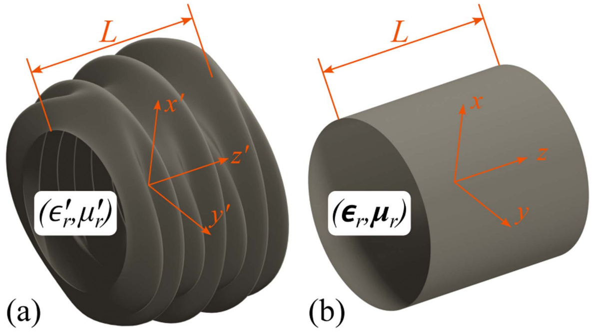

FIGURE 1. Geometric transformation. Device in the: (a) OD; (b) TD.

This novel method, whose rigorous fulfillment of the BCs is proved, enables the analysis of a wide class of devices, such as accelerator cavities [29], [30], circular tapers [6], polarizers [31], [32], and 3D-printed microwave filters [2], [33]. The proposed method may be particularly effective for the smooth shapes of 3D printed devices, which are required to have fewer structural problems in realization and improve performance as well [4].

The paper is organized as follows. In Section II, the problem is described, and the notation is introduced. In Section III, the method developed for the analysis is described and it is then applied in Section IV. Finally, the conclusion is drawn in Section V. Table 1 lists all acronyms used.

II. PROBLEM OUTLINE

Cylindrical coordinates are preferred for this problem. The coordinates of the *original domain* (OD) are (r', ϕ', z'), while those of the *transformed domain* (TD) are (r, ϕ, z). A generic CW-based device is depicted in Fig. 1(a). The ports are CWs and the profile in between is a smooth taper. The device has a length L and extends along the $z'-$axis. The device wall is a perfect electric conductor (PEC). In the OD, the device is filled with a homogeneous and isotropic medium of relative permittivity ϵ'_r and relative permeability μ'_r. The medium parameters can be different and complex, in the case of lossy media. The device lateral surface is expressed in cylindrical coordinates by $\bar{\rho}(\phi', z')$, a strictly-positive single-valued function of the angular coordinate ϕ' for each z' cross-section.

The wave equation in an arbitrarily shaped device is not separable. Therefore, a suitable transformation is applied to obtain an equivalent problem, in which the domain is a circular cylinder [Fig. 1(b)], hence it allows us to satisfy the BCs through a field expansion in terms of the CW modes. The drawback of this transformation is that the medium that fills the device of the equivalent problem presents anisotropic and inhomogeneous permittivity $\boldsymbol{\epsilon}_r$ and permeability $\boldsymbol{\mu}_r$.

The coordinate transformation from the OD to the TD is [24], [25]

$$\begin{cases} r = \frac{r'}{\bar{\rho}(\phi', z')} \\ \phi = \phi' \\ z = z' \end{cases} \tag{1}$$

where r is dimensionless and z has the same dimension of z'. The domains of the devices are

$$\Omega_{\mathrm{OD}} = [0, \bar{\rho}(\phi', z')] \times [0, 2\pi) \times [0, L] \quad \text{in the OD} \tag{2a}$$

$$\Omega_{\mathrm{TD}} = [0, 1] \times [0, 2\pi) \times [0, L] \quad \text{in the TD} \tag{2b}$$

Note that (2b) defines a cylinder [Fig. 1(b)]. The device wall is PEC in the TD too.

The fields $(\mathbf{E}', \mathbf{H}')$, solution of Maxwell equations, in the OD and the fields $(\mathbf{E}, \mathbf{H})$ in the TD are related by the Jacobian $\mathbf{J}$ of transformation (1) as [24]

$$\mathbf{E}' = \mathbf{J}^T\mathbf{E} \qquad \mathbf{H}' = \mathbf{J}^T\mathbf{H} \tag{3}$$

if the material parameters are mapped according to [24]

$$\boldsymbol{\epsilon}_r = \frac{\mathbf{J}\epsilon_r'\mathbf{J}^T}{\det(\mathbf{J})} \qquad \boldsymbol{\mu}_r = \frac{\mathbf{J}\mu_r'\mathbf{J}^T}{\det(\mathbf{J})} \tag{4}$$

where $\mathbf{J}$ is the Jacobian matrix of the transformation (1). For simplicity, throughout the paper we assume $\epsilon_r' = \mu_r' = 1$. Then, (4) becomes

$$\boldsymbol{\epsilon}_r = \boldsymbol{\mu}_r = \frac{\mathbf{J}\mathbf{J}^T}{\det(\mathbf{J})} \equiv \boldsymbol{\Lambda} \tag{5}$$

Note that if ϵ_r' and μ_r' were complex and different from one, the following treatment would remain unchanged, only the simplification (5) would not apply. The expression of $\mathbf{J}$ in cylindrical coordinates is

$$\mathbf{J} = \begin{bmatrix} \frac{1}{\bar{\rho}} & -\frac{1}{\bar{\rho}^2}\frac{\partial\bar{\rho}}{\partial\phi} & -\frac{r}{\bar{\rho}}\frac{\partial\bar{\rho}}{\partial z} \\ 0 & \frac{1}{\bar{\rho}} & 0 \\ 0 & 0 & 1 \end{bmatrix} \tag{6}$$

Matrix $\boldsymbol{\Lambda}$ (5) and its inverse $\boldsymbol{\Lambda}^{-1}$ are tensors whose expressions in cylindrical coordinates are

$$\boldsymbol{\Lambda} = \begin{bmatrix} 1 + \Theta^2 + r^2\Pi^2 & \Theta & r\Pi\Psi^{-1} \\ \Theta & 1 & 0 \\ r\Pi\Psi^{-1} & 0 & \Psi^{-2} \end{bmatrix} \tag{7}$$

$$\boldsymbol{\Lambda}^{-1} = \begin{bmatrix} 1 & -\Theta & -r\Pi\Psi \\ -\Theta & 1 + \Theta^2 & r\Pi\Theta\Psi \\ -r\Pi\Psi & r\Pi\Theta\Psi & (1 + r^2\Pi^2)\Psi^2 \end{bmatrix} \tag{8}$$

being

$$\begin{aligned} \Pi &= \Pi(\phi, z) = -\frac{\partial\bar{\rho}}{\partial z} \\ \Theta &= \Theta(\phi, z) = -\frac{1}{\bar{\rho}}\frac{\partial\bar{\rho}}{\partial\phi} \\ \Psi &= \Psi(\phi, z) = \frac{1}{\bar{\rho}} \end{aligned} \tag{9}$$

To be well defined, the partial derivatives in (9) require that $\frac{\partial\bar{\rho}}{\partial z}$ and $\frac{\partial\bar{\rho}}{\partial\phi}$ are continuous, hence the device lateral surface must be smooth with respect to both ϕ and z. The method here developed is then thought from the beginning for smooth lateral surfaces. Note that $\boldsymbol{\Lambda}_{11}$, $\boldsymbol{\Lambda}_{13}$, $\boldsymbol{\Lambda}_{31}$, $\boldsymbol{\Lambda}^{-1}_{13}$, $\boldsymbol{\Lambda}^{-1}_{31}$, $\boldsymbol{\Lambda}^{-1}_{23}$, $\boldsymbol{\Lambda}^{-1}_{32}$, $\boldsymbol{\Lambda}^{-1}_{33}$ contain a radial dependence (either linear or quadratic). This arises only in the 3D problem, while it is absent in the 2D problem [24], [25].

III. ANALYSIS METHOD

The analysis method is based on the HM reduction [18]. In particular, the field inside the cylinder in the TD is expanded in terms of CW modes, and the $z-$dependence of the fields is tackled by a 1D FEM.

The weak form formulation of the problem is worked out in Section III-A and the field expansion used is described in Section III-B. Eventually, details about solving the linear system are given in Section III-C, and the GSM is computed in Section III-D.

A. WEAK FORM FORMULATION

The electric vector wave equation is [34]

$$\nabla \times (\boldsymbol{\mu}_r^{-1}\nabla \times \mathbf{E}) - k_0^2\boldsymbol{\epsilon}_r\mathbf{E} = \mathbf{0} \tag{10}$$

where $k_0 = \omega\sqrt{\epsilon_0\mu_0}$ is the free space wavenumber, ϵ_0 (μ_0) the permittivity (permeability) of vacuum, and ω the angular frequency. The weak form [15], [35] formulation of (10) is

$$\begin{aligned} &\int_{\Omega_{\mathrm{TD}}} \nabla \times \mathbf{w} \cdot \boldsymbol{\Lambda}^{-1}\nabla \times \mathbf{E}\mathrm{d}\Omega - k_0^2 \int_{\Omega_{\mathrm{TD}}} \mathbf{w} \cdot \boldsymbol{\Lambda}\mathbf{E}\mathrm{d}\Omega \\ &= -\mathrm{j}\omega\mu_0 \int_{S_1 \cup S_2} \mathbf{w} \cdot (\mathbf{h} \times \mathbf{i}_n)\mathrm{d}S \end{aligned} \tag{11}$$

where $\mathbf{w}$ are the weighting functions, S_P with $P \in \{1, 2\}$ the port surfaces in the TD (S_1 at $z = 0$ and S_2 at $z = L$), that is, circles with radius one, $\mathbf{i}_n$ the outward unit vector at the ports ($-\mathbf{i}_z$ for S_1 and $+\mathbf{i}_z$ for S_2), $\mathbf{h}$ the impressed magnetic fields at the ports, and j the imaginary unit. In (11), $\boldsymbol{\Lambda}$ replaces $\boldsymbol{\mu}_r$ and $\boldsymbol{\epsilon}_r$ thanks to (5). A Galerkin framework is applied for discretization (weighting functions $\mathbf{w}$ equal to expansion functions, introduced later). A harmonic time dependence $\mathrm{e}^{\mathrm{j}\omega t}$ is assumed and suppressed.

The electric field wave (10) is preferred over the magnetic field wave equation. This is because the device has PEC walls and it is easier to fulfill the BCs for the electric field in the case the medium filling the waveguide is anisotropic and inhomogeneous [25]. The BCs are satisfied in the TD if and only if they are satisfied in the OD. The proof of this statement is provided in Appendix A. Consequently, if a field expansion satisfies the BCs for the electric field in the TD, then the field mapped by (3) satisfies the BCs in the OD too. The BCs for a PEC wall are given in terms of the electric field and they assume the same expression in both domains

$$\mathbf{i}_n \times \mathbf{E} = \mathbf{0} \qquad \mathbf{i}_{n'} \times \mathbf{E}' = \mathbf{0} \tag{12}$$

On the contrary, the BCs for the magnetic field assume different expressions in the two domains, because of the anisotropic and inhomogeneous medium and of the relation with the electric field

$$\mathbf{i}_n \times (\mathbf{\Lambda}^{-1}\nabla \times \mathbf{H}) = \mathbf{0} \qquad \mathbf{i}_{n'} \times (\nabla \times \mathbf{H}') = \mathbf{0} \tag{13}$$

Note that $\mathbf{\Lambda}^{-1}$ appears in the TD only. An expansion of the magnetic field in terms of the CW modes does not fulfill the BCs in the TD and then neither in the OD. As a consequence, correction terms must be added [26], increasing the complexity of the field expansion. The proper fulfillment of the BCs is an object of discussion in [5], [22] and is overlooked in [18].

B. FIELD EXPANSION

In the $r\phi-$transverse plane, the CW modes represent a suitable and convenient set for the electric field expansion, since they form a complete set [36]. Thanks to the completeness property, a series of CW modes can express the field inside the analyzed class of devices even if these have cross-sections different from CWs, hence being characterized by different modes. The $z-$dependence of the field is different from the one for uniform waveguides, based on complex exponentials, as the entries of the medium parameters depend on z. For the $z-$dependence, an expansion in terms of Lagrange polynomials to be solved with a 1D FEM technique is then applied. The unknown electric field is expanded as $\mathbf{E}(r,\phi,z) = \mathbf{E}_t(r,\phi,z) + \mathbf{E}_z(r,\phi,z)$, subscript t (z) indicates the transverse (longitudinal) component, with

$$\mathbf{E}_t(r,\phi,z) = \sum_{n=1}^{N_{\mathrm{TE}}} \mathbf{e}_{t,n}^{\mathrm{TE}}(r,\phi)\tau_n^{\mathrm{TE}}(z) + \sum_{n=1}^{N_{\mathrm{TM}}} \mathbf{e}_{t,n}^{\mathrm{TM}}(r,\phi)\tau_n^{\mathrm{TM}}(z) \tag{14a}$$

$$\mathbf{E}_z(r,\phi,z) = \sum_{n=1}^{N_{\mathrm{TM}}} \mathbf{e}_{z,n}^{\mathrm{TM}}(r,\phi)\zeta_n^{\mathrm{TM}}(z) \tag{14b}$$

where $\mathbf{e}_{t,n}^{\mathrm{TE}}$, $\mathbf{e}_{t,n}^{\mathrm{TM}}$, and $\mathbf{e}_{z,n}^{\mathrm{TM}}$ represent the real field maps for TE and TM modes, as indicated by the superscript, and N_{TE} (N_{TM}) the number of TE (TM) modes considered in the expansion. The functions $\tau_n^{\mathrm{TE}}(z)$, $\tau_n^{\mathrm{TM}}(z)$, and $\zeta_n^{\mathrm{TM}}(z)$ in (14) express the longitudinal field variation [18] and they are defined as

$$\tau_n^{\mathrm{TE}}(z) = \sum_{l=1}^{N_{l,t}} c_{n,l}^{\mathrm{TE}}\varphi_l(z) \tag{15a}$$

$$\tau_n^{\mathrm{TM}}(z) = \sum_{l=1}^{N_{l,t}} c_{n,l}^{\mathrm{TM}}\varphi_l(z) \tag{15b}$$

$$\zeta_n^{\mathrm{TE}}(z) = \sum_{l=1}^{N_{l,z}} d_{n,l}^{\mathrm{TM}}\Psi_l(z) \tag{15c}$$

where $c_{n,l}^{\mathrm{TE}}$, $c_{n,l}^{\mathrm{TM}}$, and $d_{n,l}^{\mathrm{TM}}$ are the degrees of freedom (DOFs) associated to the Lagrange polynomials $\varphi_l(z)$ and $\psi_l(z)$, and $N_{l,t}$ ($N_{l,z}$) is the number of nodes for the 1D discretization along z for the transverse (longitudinal) component. The degree of polynomial $\psi_l(z)$ is one less than the degree of polynomial $\varphi_l(z)$ [18]. Throughout the article, quadratic (linear) finite elements for the transversal (longitudinal) components are used.

The electric field expansion can be rewritten as [18]

$$\mathbf{E}_t(r,\phi,z) = \sum_{l=1}^{N_{l,t}}\sum_{n=1}^{N_M} c_{n,l}\mathbf{e}_{t,n}(r,\phi)\varphi_l(z) \tag{16a}$$

$$= \sum_{i=1}^{N_{l,t}N_M} c_{n_i,l_i}\mathbf{f}_i(r,\phi,z) \tag{16b}$$

$$\mathbf{E}_z(r,\phi,z) = \sum_{l=1}^{N_{l,z}}\sum_{n=1}^{N_{\mathrm{TM}}} d_{n,l}\mathbf{e}_{z,n}(r,\phi)\psi_l(z) \tag{16c}$$

$$= \sum_{i=1}^{N_{l,z}N_{\mathrm{TM}}} d_{n_i,l_i}\mathbf{g}_i(r,\phi,z) \tag{16d}$$

with $N_M = N_{\mathrm{TE}} + N_{\mathrm{TM}}$, and

$$\mathbf{f}_i(r,\phi,z) \equiv \mathbf{e}_{t,n_i}(r,\phi)\varphi_{l_i}(z) \tag{17a}$$

$$\mathbf{g}_i(r,\phi,z) \equiv \mathbf{e}_{z,n_i}(r,\phi)\psi_{l_i}(z) \tag{17b}$$

where no distinction is made between TE and TM modes. In (16), we switch from two indices to a single index through a suitable mapping [18]. The index i runs on both the modes and the FEM nodes. The number of DOFs to determine is

$$N_{tot} = N_M N_{l,t} + N_{\mathrm{TM}} N_{l,z} \tag{18}$$

The voltage wave normalization is applied to the transverse and longitudinal field maps in the TD

$$\int_{S_P} \mathbf{e}_{t,n}\cdot\mathbf{e}_{t,n}\mathrm{d}S = 1 \qquad \int_{S_P} \mathbf{e}_{z,n}\cdot\mathbf{e}_{z,n}\mathrm{d}S = 1 \tag{19}$$

C. LINEAR SYSTEM AND COMPUTATION OF THE MATRICES

Rewriting the field expansion (16) as

$$\mathbf{E}(r,\phi,z) = \sum_{i=1}^{N_{l,t}N_M} c_{n_i,l_i}\mathbf{f}_i(r,\phi,z) + \sum_{i=1}^{N_{l,z}N_{\mathrm{TM}}} d_{n_i,l_i}\mathbf{g}_i(r,\phi,z) \tag{20}$$

and substituting it in the weak form formulation (11), we get the following linear system

$$\left(\mathbf{A}-k_0^2\mathbf{B}\right)\begin{bmatrix}\mathbf{c}\\ \mathbf{d}\end{bmatrix} = -\mathrm{j}\omega\mu_0\begin{bmatrix}\mathbf{C}_t\\ \mathbf{0}\end{bmatrix} \tag{21}$$

where $\mathbf{c}$ and $\mathbf{d}$ are vectors collecting the unknown expansion coefficients c_{n_i,l_i} and d_{n_i,l_i}. The frequency dependence is only inside k_0 and ω, while the matrices $\mathbf{A}$ and $\mathbf{B}$ are frequency independent thanks to the voltage wave normalization (19). The generic matrix entries are [18]

$$\mathbf{A} = \begin{bmatrix}\mathbf{A}_{tt} & \mathbf{A}_{tz}\\ \mathbf{A}_{zt} & \mathbf{A}_{zz}\end{bmatrix} \tag{22a}$$

$$\mathbf{A}_{tt}(i,j) = \int_{\Omega_{\mathrm{TD}}} \nabla\times\mathbf{f}_i\cdot\mathbf{\Lambda}^{-1}\nabla\times\mathbf{f}_j\mathrm{d}\Omega \tag{22b}$$

$$\mathbf{A}_{tz}(i,j) = \int_{\Omega_{\mathrm{TD}}} \nabla\times\mathbf{f}_i\cdot\mathbf{\Lambda}^{-1}\nabla\times\mathbf{g}_j\mathrm{d}\Omega \tag{22c}$$

$$\mathbf{A}_{zt}(i,j) = \int_{\Omega_{\mathrm{TD}}} \nabla\times\mathbf{g}_i\cdot\mathbf{\Lambda}^{-1}\nabla\times\mathbf{f}_j\mathrm{d}\Omega \tag{22d}$$

$$\mathbf{A}_{zz}(i,j) = \int_{\Omega_{\mathrm{TD}}} \nabla\times\mathbf{g}_i\cdot\mathbf{\Lambda}^{-1}\nabla\times\mathbf{g}_j\mathrm{d}\Omega \tag{22e}$$

$$\mathbf{B} = \begin{bmatrix}\mathbf{B}_{tt} & \mathbf{B}_{tz}\\ \mathbf{B}_{zt} & \mathbf{B}_{zz}\end{bmatrix} \tag{23a}$$

$$\mathbf{B}_{tt}(i,j) = \int_{\Omega_{\mathrm{TD}}} \mathbf{f}_i\cdot\mathbf{\Lambda}\mathbf{f}_j\mathrm{d}\Omega \tag{23b}$$

$$\mathbf{B}_{tz}(i,j) = \int_{\Omega_{\mathrm{TD}}} \mathbf{f}_i\cdot\mathbf{\Lambda}\mathbf{g}_j\mathrm{d}\Omega \tag{23c}$$

$$\mathbf{B}_{zt}(i,j) = \int_{\Omega_{\mathrm{TD}}} \mathbf{g}_i\cdot\mathbf{\Lambda}\mathbf{f}_j\mathrm{d}\Omega \tag{23d}$$

$$\mathbf{B}_{zz}(i,j) = \int_{\Omega_{\mathrm{TD}}} \mathbf{g}_i\cdot\mathbf{\Lambda}\mathbf{g}_j\mathrm{d}\Omega \tag{23e}$$

and the vector $\mathbf{C}_t$ is defined by

$$\mathbf{C}_t(i) = \int_{S_1\cup S_2} \mathbf{f}_i\cdot(\mathbf{h}\times\mathbf{i}_n)\mathrm{d}S \tag{24}$$

Moreover, matrices $\mathbf{A}_{tt}$, $\mathbf{A}_{zz}$, $\mathbf{B}_{tt}$, $\mathbf{B}_{zz}$ are symmetric, while $\mathbf{A}_{tz} = \mathbf{A}_{zt}^T$ and $\mathbf{B}_{tz} = \mathbf{B}_{zt}^T$. In (22) and (23), the indices i and j run on both the modes and the FEM nodes. However, be aware that i and j go from 1 to $N_{l,t}N_M$ for $\mathbf{f}_i(r,\phi,z)$, while they go from 1 to $N_{l,z}N_{\mathrm{TM}}$ for $\mathbf{g}_i(r,\phi,z)$. In total, $\mathbf{A}$ and $\mathbf{B}$ have dimensions $N_{tot}\times N_{tot}$.

Expressions for $\nabla\times\mathbf{f}_i$ and $\nabla\times\mathbf{g}_i$ in (22) are [18]

$$\nabla\times\mathbf{f}_i = \varphi_{l_i}\nabla_t\times\mathbf{e}_{t,n_i} + \varphi'_{l_i}\mathbf{i}_z\times\mathbf{e}_{t,n_i} \tag{25a}$$

$$\nabla\times\mathbf{g}_i = \psi_{l_i}\nabla_t\times\mathbf{e}_{z,n_i} \tag{25b}$$

where $\varphi'_{l_i} = \frac{\mathrm{d}\varphi_{l_i}}{\mathrm{d}z}$. The explicit expressions for $\mathbf{f}_i$, $\nabla\times\mathbf{f}_i$, $\mathbf{g}_i$, and $\nabla\times\mathbf{g}_i$ are provided in Appendix B.

Details about the computation of the integrals (22) and (23) are now given. In (22) and (23), we have $\mathrm{d}\Omega = r\mathrm{d}r\mathrm{d}\phi\mathrm{d}z$. Thanks to the radial normalization, the integrals in r are the same even for different waveguide geometries, hence they can be computed numerically once and for all, stored in memory, and retrieved when necessary.

The integrals in ϕ and z deserve particular attention. They are not separable, and they are of the form

$$\int_0^L\int_0^{2\pi} \theta_{l_i}(z)h(\phi,z)\theta_{l_j}(z)\mathrm{d}\phi\mathrm{d}z \tag{26}$$

where $\theta_{l_i}(z)$ $[\theta_{l_j}(z)]$ is either φ_{l_i}, φ'_{l_i}, or ψ_{l_i} (φ_{l_j}, φ'_{l_j}, or ψ_{l_j}) and $h(\phi,z)$ is the $\phi-$ and $z-$dependent parts of the entries of $\mathbf{\Lambda}$ or $\mathbf{\Lambda}^{-1}$. To pursue a fast and efficient implementation, the function $h(\phi,z)$ is expanded as

$$h(\phi,z) = \sum_{k=1}^{N_k}\theta_{l_k}(z)h(\phi,z_k) \tag{27}$$

with $\theta_{l_k}(z)$ being the Lagrange polynomials and N_k the number of nodes used for defining the Lagrange polynomials $\theta_{l_k}(z)$. Substituting (27) into (26), we get

$$\sum_k^{N_k} u_k\int_0^L \theta_{l_i}(z)\theta_{l_j}(z)\theta_{l_k}(z)\mathrm{d}z \tag{28}$$

where

$$u_k = \int_0^{2\pi} h(\phi,z_k)\mathrm{d}\phi \tag{29}$$

There is a free choice on the degree of the Lagrange polynomials $\theta_{l_k}(z)$. Second degree is chosen for them and this is accurate in approximating $h(\phi,z)$. Then, $\theta_{l_k}(z) = \varphi_{l_k}(z)$ and $N_k = N_{l,t}$. The integrals in z in (28) are now analytical since they are the product of three Lagrange polynomials or of their derivatives (one Lagrange polynomial each for the terms indexed by i and j, and one Lagrange polynomial for the entries of $\mathbf{\Lambda}$ or $\mathbf{\Lambda}^{-1}$). They can be computed once and for all and stored in memory. Explicit expressions for (28) are given in Appendix C. Eventually, the only integrals to be computed numerically for each different geometry are the single-variable integrals in ϕ.

D. GSM COMPUTATION

From (21), the generalized impedance matrix is [18]

$$Z_v = -\mathrm{j}\omega\mu_0\mathbf{C}^T(\mathbf{A}-k_0^2\mathbf{B})^{-1}\mathbf{C} \tag{30}$$

where the subscript v indicates that voltage waves are considered due to the voltage wave normalization (19). The matrix $\mathbf{C}$ is the forcing term of size $N_{tot}\times 2N_M$. Only the $2N_M$ entries of $\mathbf{C}$ corresponding to the transversal CW modes at the ports are set to 1, the others being zero.

The power-wave GSM relates the incident power wave $\mathbf{p}^+$ to the reflected power waves $\mathbf{p}^-$ as $\mathbf{p}^- = \mathbf{S}_w\mathbf{p}^+$, where the subscript w indicates the power wave normalization. Transformation from voltage to power wave normalization requires the wave admittances. These are defined as

$$Y_i^{(P)} = \begin{cases} \frac{\gamma_i^{(P)}}{\mathrm{j}\omega\mu_0} & \text{for TE modes} \\ \frac{\mathrm{j}\omega\epsilon_0}{\gamma_i^{(P)}} & \text{for TM modes} \end{cases} \tag{31}$$

where $\gamma_i^{(P)}$ is the propagation constant of mode i at port P in the OD (port 1 at $z' = 0$ and port 2 at $z' = L$)

$$\gamma_i^{(P)} = \sqrt{\left[k_{c,i}^{(P)}\right]^2 - k_0^2} \tag{32}$$

with $k_{c,i}^{(P)}$ the mode eigenvalue, whose expression is provided in Appendix B. The wave impedance is the inverse of the wave admittance, $Z_i^{(P)} = 1/Y_i^{(P)}$. Eventually, the power-wave GSM is computed as [11]

$$\mathbf{S}_w = \sqrt{\mathbf{Y}_m}\,(\mathbf{Z}_v + \mathbf{Z}_m)^{-1}\,(\mathbf{Z}_v - \mathbf{Z}_m)\,\sqrt{\mathbf{Z}_m} \tag{33}$$

where $\mathbf{Z}_m$ and $\mathbf{Y}_m$ are diagonal matrices containing the wave impedances and admittances and their square roots are element-wise.

In the present work, the ports are always CWs. Then, calculations are easier than in [18], where the Jacobian of the transformation at the ports accounts for the different aspect ratios of the rectangular ports.

IV. RESULTS

The following examples are considered: (A) linear taper; (B) sinusoidal taper; (C) circle-ellipse-circle taper; (D) circle-bilobate-circle taper; (E) third-degree polynomial taper.

The results of HM are compared against full-wave simulations (3D FEM from CST Microwave Studio [16]) and, for example (D), against measurements, also. Convergence analysis [number of modes considered in the expansion (14)] is also performed. The accuracy of the frequency domain solver from CST is the following: convergence on all scattering parameters less than 0.02 in linear unit (−34.0 dB) and the ratio γ/k_0 at ports less than 0.005.

For 1D discretization, evenly spaced nodes are chosen, increasing computational efficiency (Appendix C). The number of intervals for the 1D FEM is

$$N_t = \lceil L/\nu \rceil \tag{34}$$

with L the length of the device and

$$\nu = \frac{v_f}{f_m \xi} \tag{35}$$

where v_f is the light speed in the medium filling the waveguide in the OD, f_m is the maximum analysis frequency, and ξ is called mesh factor. Unless otherwise stated, $\xi = 10$. Note that v_f/f_m is the shortest analysis wavelength. The length of the Lagrange basis functions is $a = L/N_t$ and it is at least $\xi-$times shorter than the shortest wavelength. The number of intervals (34) relates to the number of nodes $N_{l,z}$ and $N_{l,t}$ as

$$N_{l,z} = N_t + 1 \qquad N_{l,t} = 2N_t + 1 \tag{36}$$

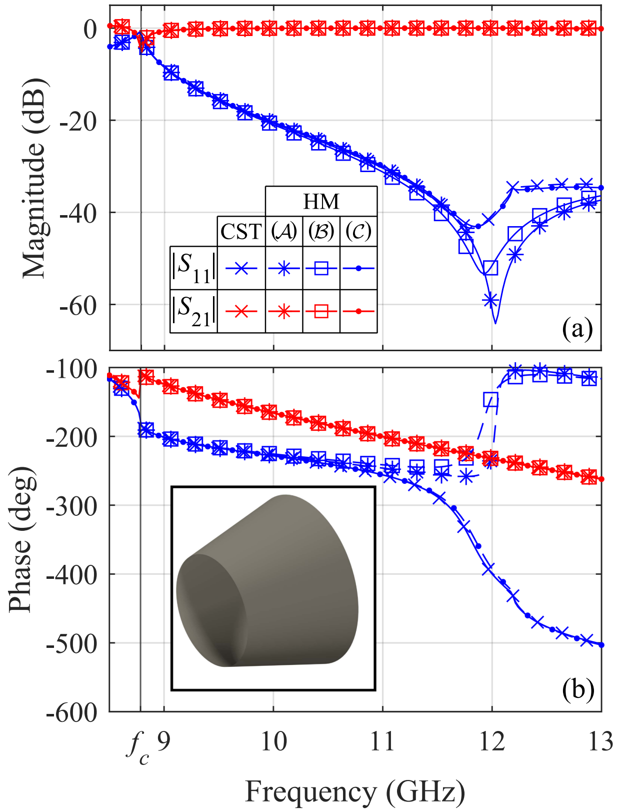

FIGURE 2. Scattering parameters for the fundamental mode (TE$_{11}$) for a linear taper (narrower port only): (a) magnitude; (b) phase. In the legend, ($\mathcal{A}$), ($\mathcal{B}$), and ($\mathcal{C}$) indicate the mode sets: ($\mathcal{A}$) TE$_{11}$, ($\mathcal{B}$) TE$_{11}$, TE$_{12}$, TE$_{13}$, ($\mathcal{C}$) TE$_{11}$, TE$_{12}$, TE$_{13}$, TM$_{11}$, TM$_{12}$, TM$_{13}$. In the horizontal axis, f_c indicates the cutoff frequency of the TE$_{11}$ mode at the narrower port.

A. LINEAR TAPER

The first example is a linear taper whose expression is

$$\bar{\rho}(\phi', z') = R_1 + (z'/L)(R_2 - R_1) \tag{37}$$

with $R_1 = 10$ mm, and $R_2 = 15$ mm, and $L = 20$ mm. The taper is analyzed in the frequency range 8.5 − 13 GHz, and the shortest wavelength is $\lambda = 23.06$ mm, then $L = 0.87\lambda$.

Three sets of modes are considered: ($\mathcal{A}$) TE$_{11}$, ($\mathcal{B}$) TE$_{11}$, TE$_{12}$, TE$_{13}$, ($\mathcal{C}$) TE$_{11}$, TE$_{12}$, TE$_{13}$, TM$_{11}$, TM$_{12}$, TM$_{13}$. The number of intervals is 9 and the DOFs (18) for each mode set per frequency point are ($\mathcal{A}$) 19, ($\mathcal{B}$) 57, and ($\mathcal{C}$) 144. The device is symmetric with respect to the $x'-$ and $y'-$axes. Then, it is analyzed considering a PEC [perfect magnetic conductor (PMC)] plane along the $x-$axis and a PMC (PEC) along the $y-$axis both in the HM and CST. For more details on mode symmetries in the TO approach, see [26] and Appendix B. In addition, the device features a 90°−rotation symmetry with respect to the $z'-$axis, so there is no distinction between the polarizations.

In Fig. 2, the scattering parameters for the linear taper are plotted. For brevity, only the results for the narrower port with radius R_1 are shown. Regarding the magnitude, the mode set ($\mathcal{A}$) delivers acceptable results up to −30 dB, while the mode set ($\mathcal{B}$) up to −40 dB. For smaller magnitudes, their results

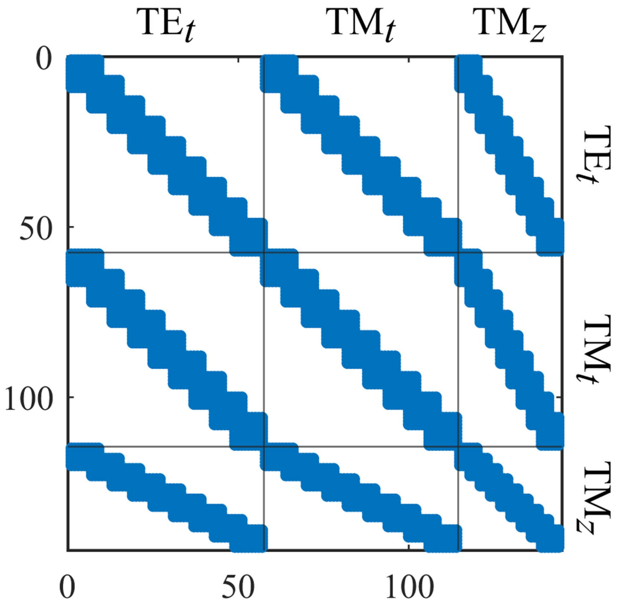

FIGURE 3. Filling of the matrix **A** for the results in Fig. 2 [mode set ($\mathcal{C}$)].

start to diverge from the CST reference. However, the results of the mode set ($\mathcal{C}$) replicate well the reference results in the entire frequency range. Regarding the phase, no difference can be appreciated for the phase of S_{21} for all mode sets. On the other hand, for the phase of S_{11} the results from mode sets ($\mathcal{A}$) and ($\mathcal{B}$) deviate from the reference results starting at about 11 GHz and for greater frequencies they present an opposite behavior with respect to the reference solution, that is, they increase instead of decreasing. The reason for this is that the results for mode sets ($\mathcal{A}$) and ($\mathcal{B}$) encompass the origin on the Smith chart, while those for the reference solution do not. As for the magnitude, the phase results of the mode set ($\mathcal{C}$) agree well with the CST ones in the entire frequency range.

In Fig. 3, the nonzero entries of the matrix **A** for the mode set ($\mathcal{C}$) are shown. The results for matrix **B** are analogous, and hence they are omitted. The blocks of the matrix are, in order, transverse component TE modes, transverse component TM modes, and longitudinal component TM modes. The ordering of the submatrix reflects the subdivision (22). In addition, only elements close to the diagonals of each submatrix are nonzero since only Lagrange polynomials defined on the same interval or adjacent intervals interact (Appendix C). The dimensions of **A** are 144 × 144 for a total of 20736 entries, but only 4504 entries are nonzero (matrix density $\eta = 21.7\%$). Suitable routines for sparse matrices can thus be applied. The density η decreases for electrically larger problems, as we will see next.

B. SINUSOIDAL TAPER

A sinusoidal taper connecting two CWs with different radii is now considered. Its lateral surface is expressed by

$$\bar{\rho}(\phi', z') = R_1 + (R_2 - R_1) \sin\left(\frac{z'\pi}{2L}\right) \tag{38}$$

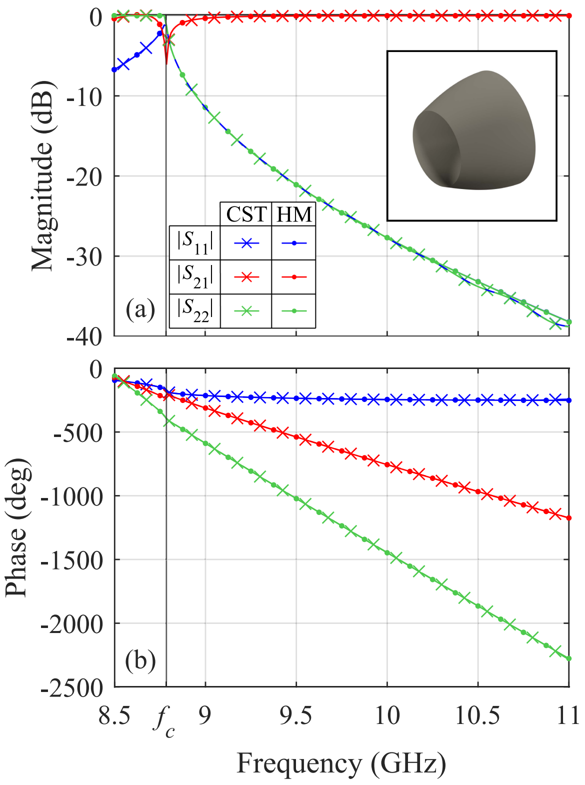

FIGURE 4. Scattering parameters of the TE_{11} mode for a sinusoidal taper: (a) magnitude; (b) phase. Along the horizontal axis, f_c indicates the cutoff frequency of TE_{11} mode at the narrower port.

with $R_1 = 10$ mm, $R_2 = 25$ mm, and $L = 300$ mm. The taper is analyzed in the frequency range $8.5 - 11$ GHz, and the shortest wavelength is $\lambda = 27.25$ mm, then $L = 11.01\lambda$. The electrical length is two orders of magnitude greater than in the previous example.

The set of modes is TE_{11}, TE_{12}, TE_{13}, TM_{11}, TM_{12}, TM_{13}. The number of intervals is 111 and the DOFs per frequency point are 1674. The device is symmetric with respect to the $x'-$ and $y'-$axes and presents a $90^\circ-$rotation symmetry with respect to the $z'-$axis.

The scattering parameters for the TE_{11} mode at both ports are compared in Fig. 4. The agreement between the curves is apparent, even at the cutoff frequency of the narrower port, where the variation of the scattering parameters against frequency is faster. A slight discrepancy arises for magnitude values less than -30 dB, but it can be easily attributed to the limited accuracy of the CST solutions for small magnitudes. Regarding the phase, the large absolute variations are due to the relatively large value for the electrical length of the device.

C. CIRCLE-ELLIPSE-CIRCLE TAPER

The device is a circle-ellipse-circle taper described by

$$\bar{\rho}(\phi', z') = \left(\left(\frac{\cos(\phi')}{Z_1(z')}\right)^2 + \left(\frac{\sin(\phi')}{Z_2(z')}\right)^2\right)^{-1/2} \tag{39}$$

with $Z_1(z') = R_1 + R_2\sin^2(\pi z'/L)$, $Z_2(z') = R_1 = 10$ mm, $R_2 = 5$ mm, $L = 20$ mm. The cross-section of the device at each longitudinal coordinate is an ellipse. The taper is analyzed in the frequency range $8.5 - 11$ GHz, and the shortest wavelength is $\lambda = 27.25$ mm, then $L = 0.73\lambda$.

Convergence analysis is performed. First, $P = Q = 3$ and second, $P = Q = 7$, where P (Q) denotes the maximum value of the angular index (zero of the Bessel function or its derivative). The modes that are considered in the two cases are: TE_{pq}, TM_{pq} for $p \in [1, 3]$ and $q \in [1, 2, 3]$ for $P = Q = 3$ (12 modes totally) and TE_{pq}, TM_{pq} for $p \in [1, 3, 5, 7]$ and $q \in [1, 2, 3, 4, 5, 6, 7]$ for $P = Q = 7$ (56 modes totally). The number of intervals is 8 and the DOFs per frequency point are 258 for $P = Q = 3$ and 1204 for $P = Q = 7$.

The device exhibits a twofold symmetry along the $x'-$ and $y'-$axes. Despite this, the device does not present a 90°−rotation symmetry with respect to the $z'-$axis. Then, the two orthogonal polarizations [Fig. 5(a)] along the $x'-$axis (H-pol.) and $y'-$axis (V-pol.) for the TE_{11} CW mode experience a different propagation through the device. The magnitudes of the scattering parameters for the TE_{11} mode and both polarizations are shown in Fig. 5(b)–(c). The magnitudes of the scattering parameters are greater than 0 dB below the cutoff frequency, since the ports are placed at the ends of the taper and, consequently, the non-propagating modes may be reflected or transmitted with a magnitude greater than the impinging one. Note the resonance exhibited by $|S_{11}|$ for the H-pol. in Fig. 5(b) at 9.2 GHz. Although for $P = Q = 3$ the HM results differ from those of CST, no difference can be appreciated for $P = Q = 7$. All the other curves, characterized by a less sharp variation, are satisfactory even for $P = Q = 3$. For completeness, Fig. 5(d) shows the phase difference for the transmission coefficients of the two polarizations (phase of the H-pol. minus the phase of the V-pol.).

Note from (39) and the inset in Fig. 5(c), that the shape of the device resembles that of modern 3D-printed resonators [4]. Thus, the proposed method may be potentially applied to model such complex shapes.

D. CIRCLE-BILOBATE-CIRCLE TAPER

The next example is taken from the literature [31]. It is a polarizer realized by a circle-bilobate-circle taper used in high-power microwave applications [1]. The expression for the waveguide lateral surface is

$$\bar{\rho}(\phi', z') = R + r\sin^2\left(\frac{\pi z'}{L}\right)\cos(n\phi') \qquad (40)$$

where R is the baseline radius, r the offset of the lobes, L the length of the device, and $n = 2$ the number of lobes. For r/R small, $R + r\cos(n\phi')$ resembles an ellipse [31].

Two devices based on (40) are analyzed and reported in [31]. Their parameters are: (s, for short) $R = 5$ mm, $r = 0.917$ mm, $L = 48$ mm; (ℓ, for long) $R = 13.895$ mm, $r = 1.99$ mm, $L = 1$ m. The frequency range is $22 - 40$ GHz,

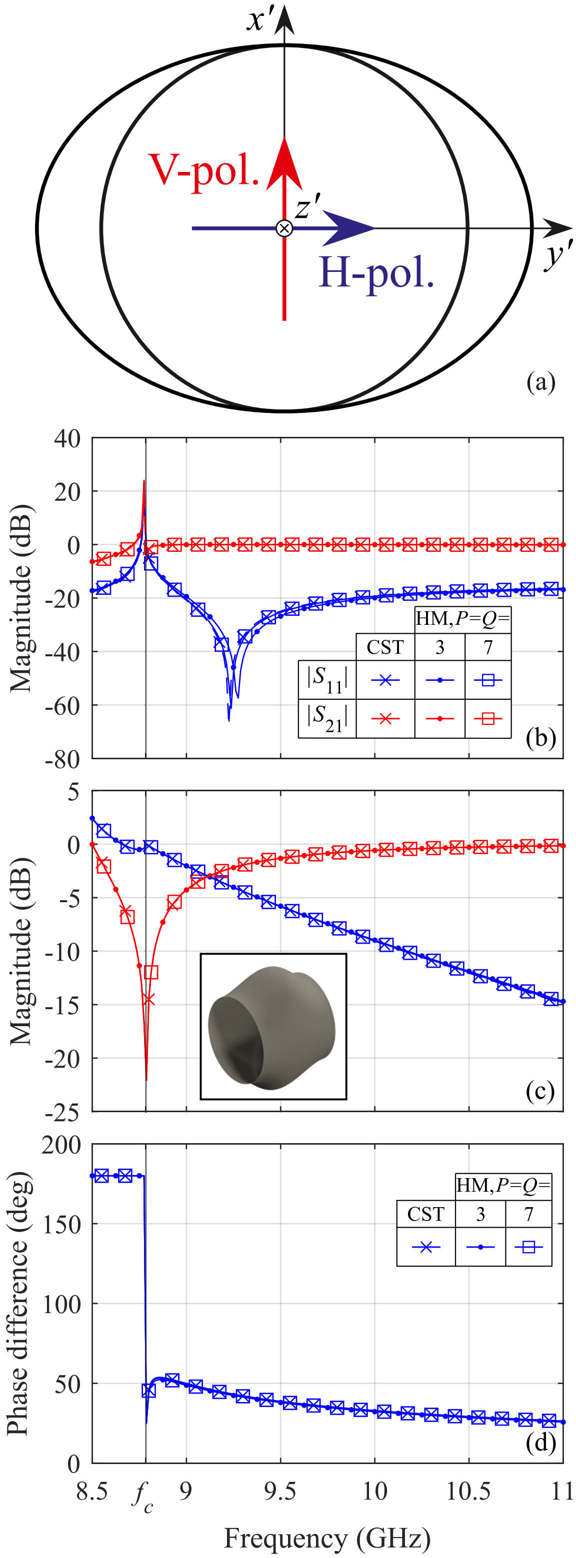

FIGURE 5. Circular-elliptical-circular taper: (a) orientation of the device and definition of the polarizations; the magnitude of the scattering parameters of TE_{11} mode for (b) horizontal and (c) vertical polarizations; (d) phase difference for the two TE_{11} polarizations. (b) and (c) share the same legend. On the frequency axis, f_c indicates the cutoff frequency of TE_{11} at the ports.

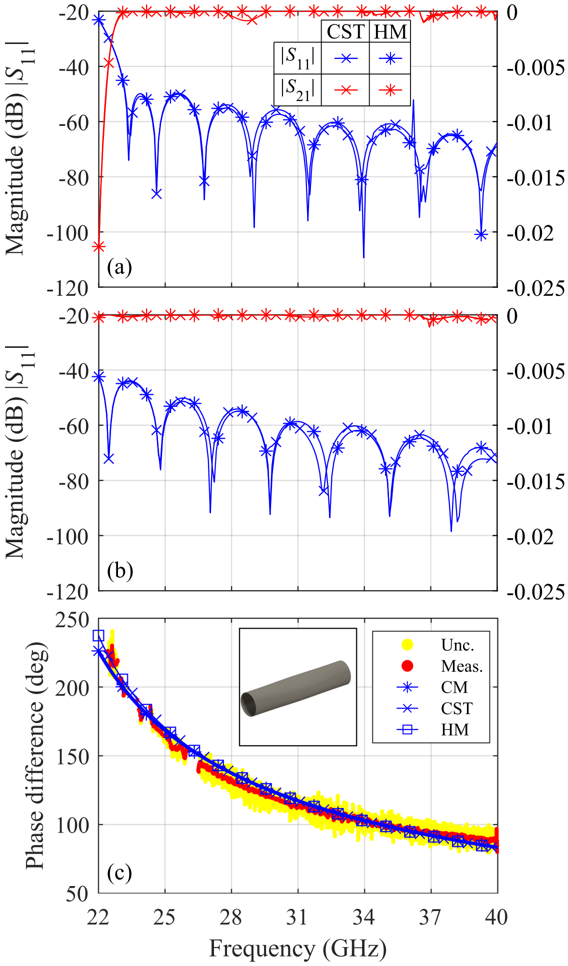

FIGURE 6. **Short polarizer. The magnitude of the scattering parameters for the TE$_{11}$ mode: (a) horizontal and (b) vertical polarizations; (c) phase difference for the transmission coefficient. In the legend of (c), Unc. stands for uncertainty, Meas. stands for measurements, and CM for the coupled mode theory used in [31].**

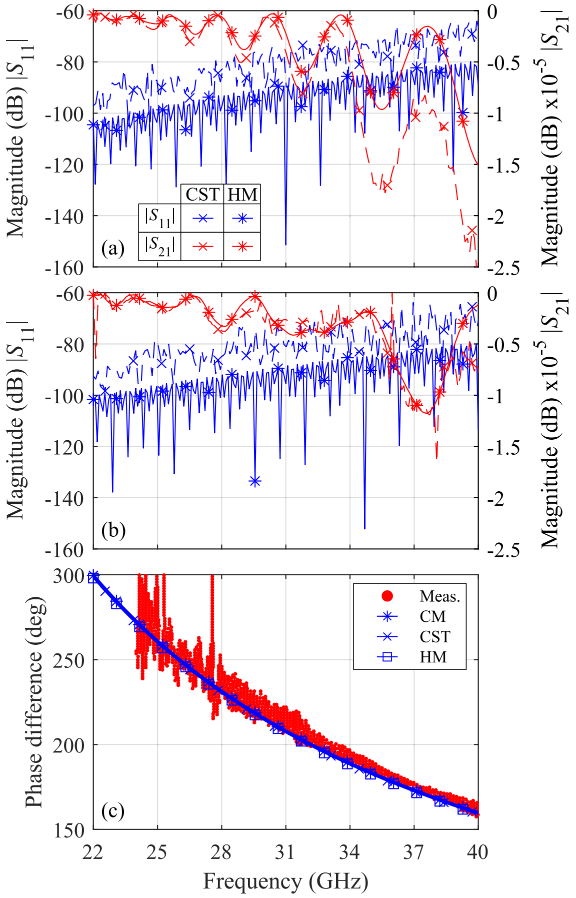

FIGURE 7. **Long polarizer. The magnitude of the scattering parameters for the TE$_{11}$ mode: (a) horizontal and (b) vertical polarizations; (c) phase difference for the transmission coefficient. In the legend of (c), Meas. stands for measurements, and CM for the coupled mode theory used in [31].**

covering part of the $K-$band and the entire K_a-band, and the shortest wavelength is $\lambda = 7.49$ mm. Then, the lengths of the polarizers are 6.40 λ for (s) and 133.43 λ for (ℓ). The modes considered for the two polarizers are: TE$_{pq}$, TM$_{pq}$ for $p \in [1, 3]$ and $q \in [1, 2, 3]$, $P = Q = 3$ (12 modes in total). The number of intervals and the DOFs are 65 and 1968 for (s); 1335 and 40068 for (ℓ).

In Figs. 6 and 7, the magnitudes of the scattering parameters and the phase differences for the transmission coefficients of the two TE$_{11}$ modes are reported against the measurements [31] and the CM method used in [31]. Note that no measurement is available in the literature for the magnitudes of the scattering parameters. The HM and CST results agree well for the short polarizer. The long polarizer has a reflection coefficient with many nulls because of its greater electrical length. For this polarizer, the CST and HM results for the reflection coefficient are noisy. However, in the entire frequency range $|S_{11}|$ is less than -60 dB, a value smaller than the accuracy set in the CST simulations. Regarding $|S_{21}|$, HM and CST results agree well, except for a small discrepancy at higher frequencies for the horizontal polarization, which however is also less than the accuracy set in CST simulations. An apparent agreement between the results of CM, CST, HM, and measurements is obtained instead for the phase difference. The HM solution of the method proposed is more accurate than the CM one at low frequency since this represents a limitation for the CM method [31].

E. THIRD-DEGREE POLYNOMIAL TAPER

To challenge the validity of the proposed method in case a taper close to a discrete step is considered, the following taper with a third-degree polynomial profile is analyzed

$$\bar{\rho}(\phi', z') = \begin{cases} R_1 & \text{if } -\frac{L}{2} \le z' \le -\frac{\delta}{2} \\ -2h\left(\frac{z'}{\delta}\right)^3 + \frac{3}{2}h\left(\frac{z'}{\delta}\right) + R & \text{if } -\frac{\delta}{2} \le z' \le +\frac{\delta}{2} \\ R_2 & \text{if } +\frac{\delta}{2} \le z' \le +\frac{L}{2} \end{cases} \tag{41}$$

where R_1 (R_2) is the radius of the smaller (larger) CW, $h = R_2 - R_1$ the height of the step, $R = R_1 + \frac{h}{2} = R_2 - \frac{h}{2}$, and δ

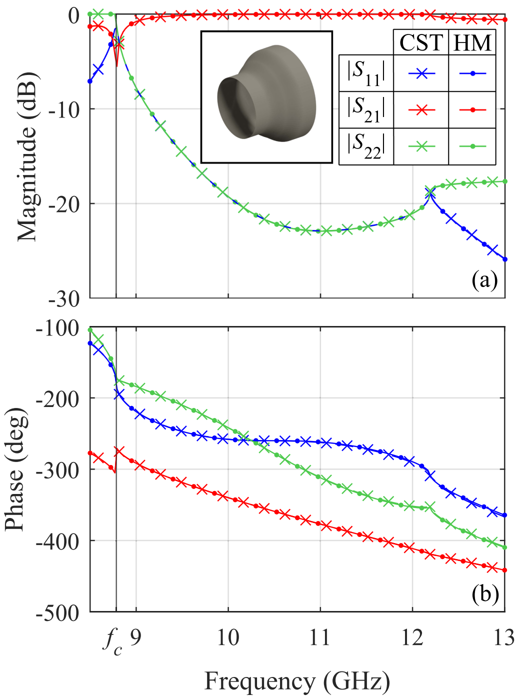

FIGURE 8. Scattering parameters of the TE_{11} mode for the third-degree polynomial taper with $\delta = 10$ mm: (a) magnitude; (b) phase. Along the horizontal axis, f_c indicates the cutoff frequency of TE_{11} mode at the narrower port.

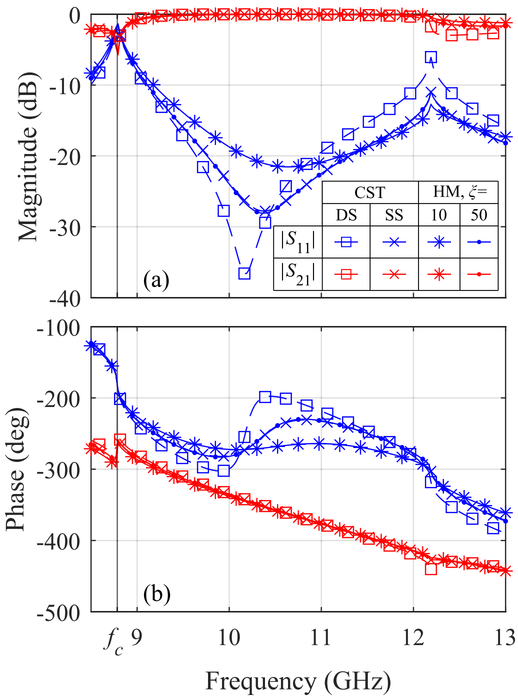

FIGURE 9. Scattering parameters of the TE_{11} mode (narrower port only) for the third-degree polynomial taper with $\delta = 2.5$ mm and a discrete step ($\delta = 0$): (a) magnitude; (b) phase. In the legend, DS (SS) stands for discrete (smooth) step. The HM results are provided for $\xi = 10$ and $\xi = 50$. Along the horizontal axis, f_c indicates the cutoff frequency of TE_{11} mode at the narrower port.

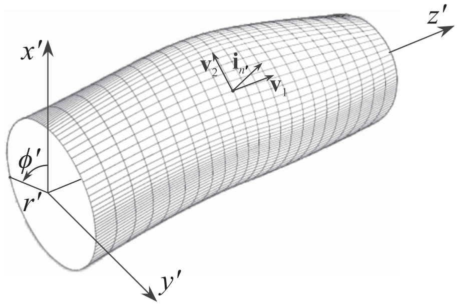

FIGURE 10. Definition of the tangent vectors in (46).

the length of the taper along z'. The taper extends from $-\delta/2$ to $+\delta/2$. At the ends of the taper we have

$$\bar{\rho}(\phi', z' = -\delta/2) = R_1 \tag{42a}$$

$$\bar{\rho}(\phi', z' = +\delta/2) = R_2 \tag{42b}$$

$$\left.\frac{\partial \bar{\rho}(\phi', z')}{\partial z'}\right|_{z'=\pm\delta/2} = 0 \tag{42c}$$

The values of the parameters are $R_1 = 10$ mm, $R_2 = 15$ mm, $L = 20$ mm. The parameter δ is the object of the study as it controls the steepness of the taper. If δ tends to zero, the taper tends to a discrete step, which could be solved by MM. In the following, we consider the cases $\delta = 10$ mm and $\delta = 2.5$ mm. As for example (A), the frequency range for the analysis is $8.5 - 13$ GHz, and the shortest wavelength $\lambda = 23.06$ mm, then $L = 0.87\lambda$. The modes used are TE_{pq}, TM_{pq} for $p \in [1, 3, 5, 7]$ and $q \in [1, 2, 3, 4, 5, 6, 7]$ (56 modes totally), as for the case $P = Q = 7$ in example (C).

The scattering parameters for the case $\delta = 10$ mm ($\delta = 2.5$ mm) are shown in Figs. 8 and 9. For the case $\delta = 10$ mm, a mesh factor $\xi = 15$ is considered as it provides more accurate results than $\xi = 10$. However, the curves for $\xi = 10$ are not reported in Fig. 8 as they are almost indistinguishable from those for $\xi = 15$. A greater value of ξ implies shorter basis domains and more DOFs. In particular, for ξ equal to 10, 15, and 55, the number of intervals are 9, 14, and 44, and the DOFs are 1344, 2044, and 6244, respectively. In Fig. 8, there is a perfect agreement between the results from CST and HM, both for the magnitude and phase. For the case $\delta = 2.5$ mm, the results obtained considering $\xi = 10$ and $\xi = 50$ are compared. In Fig. 9, the HM results with $\xi = 10$ completely fail in replicating the CST results, while the HM results with $\xi = 50$ perfectly agree with the CST results. In Fig. 9, curves are also drawn for the case of a discrete step ($\delta = 0$ mm). They show that even if a short step with $\delta = 2.5$ mm is considered there is still a difference with the discrete step.

F. PERFORMANCE COMPARISON

The performance of the HM solution is now compared with the CST one. As a key indicator, the number of DOFs is considered. In fact, the bottleneck of both HM and CST is the solution of the linear systems (30) and (33) and the solution

TABLE 2. Performance Comparison for CST and HM in Terms of DOFs

Example	CST DOFs	HM DOFs	η (%)
A	13828	144 mode set ($\mathcal{C}$)	21.7
B	33554	1674	2.0
C	9917*	1204 ($P = Q = 7$)	24.3
D (s)	17251*	1968	3.3
D (ℓ)	4945799*	40068	0.2
E ($\delta = 10$ mm)	15524	2044 ($\xi = 15$)	14.6
E ($\delta = 2.5$ mm)	58900	6244 ($\xi = 50$)	4.9

For the HM, the matrix densities η of matrix A are also shown. For CST, the * indicates that the mean between the two polarizations is considered. For HM, only the numbers of DOFs corresponding to the most accurate solution are provided.

time scales with the size of the problem, that is, with the number of DOFs considered.

In Table 2, the numbers of DOFs for the analyzed examples are reported. Across the examples considered, the number of DOFs for the CST solutions is between one and two orders of magnitude grater than for the HM solution, thus showing the gain in computation complexity. Table 2 even reports the matrix densities of matrix **A**. They are always lower than a quarter and for a fixed mode set they decrease for increasing DOFs due to the 1D FEM used for the longitudinal problem.

V. CONCLUSION

A novel full-wave analysis method for CW-based devices is introduced. The method is based on TO, HM reduction, and 1D FEM. First, the original waveguide filled with a homogeneous and isotropic dielectric is mapped into a circular cylinder with an inhomogeneous and anisotropic medium. Second, through a hierarchical model reduction the electric field is expanded in terms of CW modes on the transverse plane, and the longitudinal field dependence is addressed by a 1D FEM. The method proves to be: rigorous, as it fulfills the BCs exactly; accurate, as shown by the good agreement between its results and those from a full-wave simulator and measurements; efficient, as the DOFs of the proposed method are between one and two orders of magnitude less than those required by 3D FEM solution from commercial software.

The limitations of the applicability of the method are: (a) the ports must be CWs; (b) the device lateral surface $\bar{\rho}(\phi', z')$ must be a strictly-positive single-valued function with respect to both ϕ' and z'; (c) the device lateral surface must be smooth, that is, the partial derivatives of $\bar{\rho}(\phi', z')$ with respect to both entries are continuous.

As the next step, we are interested in expanding the method to devices with ports of arbitrary cross-sections. An additional development is to expand the method to multiply connected domains, such as stripline, so that tapers, such as those of transverse electromagnetic cells [37], [38], [39] can be analyzed full-wave. Not least, it would be of interest to define the device lateral surface by cross-sections at the nodes. Then, it would not be needed to have an analytical expression for the $z-$dependence, provided that the quantities (9) are known as functions of ϕ at the nodes. Eventually, it would be of help to develop a non-uniform sampling along z so to increase the mesh density only where the device lateral surface is steeper.

APPENDIX A
ON THE BOUNDARY CONDITIONS

The statement reads: *BCs are satisfied in the TD if and only if they are satisfied in the OD*. This is an "*if and only if*" condition, thus both directions must be proved. The unprimed quantities refer to the TD, while the primed ones refer to the OD. In this appendix, $\mathcal{C}$ is the device lateral surface, that is

$$\mathcal{C}' = [\bar{\rho}(\phi', z')] \times [0, 2\pi) \times [0, L] \quad \text{in the OD} \tag{43a}$$

$$\mathcal{C} = [1] \times [0, 2\pi) \times [0, L] \quad \text{in the TD} \tag{43b}$$

A. THE BCS ARE SATISFIED IN THE TD

Hypothesis: $\mathbf{i}_n \times \mathbf{E} = \mathbf{0}$ for $(r, \phi, z) \in \mathcal{C}$ (that is, BCs are satisfied in the TD)

Thesis: $\mathbf{i}_{n'} \times \mathbf{E}' = \mathbf{0}$ for $(r', \phi', z') \in \mathcal{C}'$ (that is, BCs are satisfied in the OD)

Proof: The hypothesis writes $\mathbf{0} = \mathbf{i}_n \times \mathbf{E} = \mathbf{i}_r \times \mathbf{E} = -\mathbf{i}_\phi E_z + \mathbf{i}_z E_\phi \Rightarrow E_z = 0, E_\phi = 0$. To get $\mathbf{i}_{n'}$ and $\mathbf{E}'$ from $\mathbf{i}_n$ and $\mathbf{E}$ on the device lateral surface ($r' = \bar{\rho}$ in the OD and $r = 1$ in the TD), respectively, we left-multiply $\mathbf{i}_n$ and $\mathbf{E}$ by the transpose of the Jacobian (6) obtaining

$$\mathbf{i}_{n'} = \frac{1}{\sigma}\left(\mathbf{i}_{r'} + \Theta \mathbf{i}_{\phi'} + \Pi \mathbf{i}_z\right) \tag{44}$$

$$\begin{aligned} \mathbf{E}' &= \Psi E_r \mathbf{i}_{r'} + \Psi\left(\Theta E_r + E_\phi\right)\mathbf{i}_{\phi'} + (\Pi \Psi E_r + E_z)\,\mathbf{i}_{z'} \\ &= \Psi E_r \mathbf{i}_{r'} + \Theta \Psi E_r \mathbf{i}_{\phi'} + \Pi \Psi E_r \mathbf{i}_{z'} \end{aligned} \tag{45}$$

where $\sigma = \sqrt{1 + \Theta^2 + \Pi^2}$ and the last equality in (45) derives from $E_z = 0, E_\phi = 0$. Eventually, the cross product $\mathbf{i}_{n'} \times \mathbf{E}' = \mathbf{0}$ vanishes (calculations are omitted for brevity), proving that the BCs for the electric field are satisfied in the OD too.

B. THE BCS ARE SATISFIED IN THE OD

Hypothesis: $\mathbf{i}_{n'} \times \mathbf{E}' = \mathbf{0}$ and $(r', \phi', z') \in \mathcal{C}'$

Thesis: $\mathbf{i}_n \times \mathbf{E} = \mathbf{0}$ and $(r, \phi, z) \in \mathcal{C}$

To rewrite the hypothesis in a more readable form, the vector $\mathbf{i}_{n'}$ is computed explicitly. To do so, let us parameterize the device lateral surface in Cartesian coordinates: $\phi' \in [0, 2\pi), z' \in [0, L] \rightarrow \Gamma_C = (\bar{\rho}(\phi')\cos(\phi'), \bar{\rho}(\phi')\sin(\phi'), z')$. The tangent plane is the plane spanned by the vectors (Fig. 10)

$$\mathbf{v}_1 = \frac{\partial \Gamma_C}{\partial z'} \qquad \mathbf{v}_2 = \frac{\partial \Gamma_C}{\partial \phi'} \tag{46}$$

and the orthogonal vector is $\mathbf{i}_{n'} = \mathbf{v}_1 \times \mathbf{v}_2$, which in cylindrical coordinates assumes the expression (44). The BC $\mathbf{i}_{n'} \times \mathbf{E}' = \mathbf{0}$ implies

$$\Theta E'_z - \Pi E'_\phi = 0 \quad \Pi E'_r - E'_z = 0 \quad E'_\phi - \Theta E'_r = 0 \tag{47}$$

To get $\mathbf{i}_n$ and $\mathbf{E}$ from $\mathbf{i}_{n'}$ and $\mathbf{E}'$, respectively, we left-multiply by the inverse of the transpose of the Jacobian (6) on the device lateral surface ($r = 1$) obtaining $\mathbf{i}_n = \mathbf{i}_r$ and

$$\mathbf{E} = \Psi^{-1} E'_r \mathbf{i}_r + \Psi^{-1}\left(E'_\phi - \Theta E'_r\right)\mathbf{i}_\phi + \left(E'_z - \Pi E'_r\right)\mathbf{i}_z \tag{48}$$

Eventually, the vector product

$$\mathbf{i}_n \times \mathbf{E} = \left(\Pi E'_r - E'_z\right)\mathbf{i}_\phi + \Psi^{-1}\left(E'_\phi - \Theta E'_r\right)\mathbf{i}_z \tag{49}$$

vanishes thanks to (47).

APPENDIX B
MODES IN THE CW

The radius of the waveguide in the TD is one thanks to (1). The CW modes normalized as (19) are

$$\mathbf{e}_z^{\mathrm{TM}} = A_z^{\mathrm{TM}} J_p(\chi_{pq} r)\eta_p^\iota(\phi)\mathbf{i}_z \tag{50a}$$

$$\mathbf{e}_t^{\mathrm{TM}} = A_t^{\mathrm{TM}}\left(\chi_{pq} J'_p(\chi_{pq} r)\eta_p^\iota(\phi)\mathbf{i}_r + \frac{p}{r} J_p(\chi_{pq} r)\eta_p^{\iota'}(\phi)\mathbf{i}_\phi\right) \tag{50b}$$

$$\mathbf{e}_t^{\mathrm{TE}} = A_t^{\mathrm{TE}}\left(-\frac{p}{r} J_p(\tilde{\chi}_{pq} r)\eta_p^{\iota'}(\phi)\mathbf{i}_r + \tilde{\chi}_{pq} J'_p(\tilde{\chi}_{pq} r)\eta_p^\iota(\phi)\mathbf{i}_\phi\right) \tag{50c}$$

where χ_{pq} ($\tilde{\chi}_{pq}$) is the $q-$th zero of the Bessel function of order p, $J_p(\chi_{pq}) = 0$ [of the derivative of the Bessel function of order p, $J'_p(\tilde{\chi}_{pq}) = 0$], A_z^{TM}, A_t^{TM}, and A_t^{TE} are the normalization constants

$$A_z^{\mathrm{TM}} = \left\{\varepsilon_p \pi \left[-J_{p-1}(\chi_{pq}) J_{p+1}(\chi_{pq})\right]\right\}^{-1/2} \tag{51a}$$

$$A_t^{\mathrm{TM}} = \frac{1}{\chi_{pq}} A_z^{\mathrm{TM}} \tag{51b}$$

$$A_z^{\mathrm{TE}} = \frac{1}{\tilde{\chi}_{pq}}\left\{\varepsilon_p \pi \left[J_p(\tilde{\chi}_{pq})^2 - J_{p-1}(\tilde{\chi}_{pq}) J_{p+1}(\tilde{\chi}_{pq})\right]\right\}^{-1/2} \tag{51c}$$

being

$$\varepsilon_p = \begin{cases} 1 & \text{if } p = 0 \\ 1/2 & \text{if } p \neq 0 \end{cases} \tag{52}$$

and $\eta_p^\iota(\phi)$ and $\eta_p^{\iota'}(\phi)$ are the trigonometric functions used for the angular dependence of the fields

$$\eta_p^\iota(\phi) = \begin{cases} \cos(p\phi) & \text{if } \iota = e \\ \sin(p\phi) & \text{if } \iota = o \end{cases} \tag{53}$$

and the prime indicates the derivative with respect to ϕ. Symmetries along the $x-$ and $y-$axes are treated as in [26]. In particular, $\iota = e$ indicates a PMC (PEC) symmetry along the $x-$axis for TM (TE) modes, while $\iota = o$ a PEC (PMC) symmetry along the $x-$axis for TM (TE) modes. The symmetry along the $y-$axis is handled through index p [26].

The CW mode eigenvalue $k_{c,i}^{(P)}$ needed in (32) is

$$k_{c,i}^{(P)} = \frac{\tilde{\chi}_{p_i q_i}}{R^{(P)}} \text{for TE modes} \tag{54a}$$

$$k_{c,i}^{(P)} = \frac{\chi_{p_i q_i}}{R^{(P)}} \text{for TM modes} \tag{54b}$$

where $R^{(P)}$ is the radius of the CW at port P in the OD.

Eventually, the functions $\mathbf{f}_i$ and $\mathbf{g}_i$ in (20) write

$$\mathbf{f}_i^{\mathrm{TE}} = A_t^{\mathrm{TE}}\Big[\varphi_{l_i}(z)\Big(-\frac{p}{r} J_p(\tilde{\chi}_{p_i q_i} r)\eta_p^{\iota'}(\phi)\mathbf{i}_r + \tilde{\chi}_{p_i q_i} J'_p(\tilde{\chi}_{p_i q_i} r)\eta_p^\iota(\phi)\mathbf{i}_\phi\Big)\Big] \tag{55a}$$

$$\mathbf{f}_i^{\mathrm{TM}} = A_t^{\mathrm{TM}}\Big[\varphi_{l_i}(z)\Big(\chi_{p_i q_i} J'_p(\chi_{p_i q_i} r)\eta_p^\iota(\phi)\mathbf{i}_r + \frac{p}{r} J_p(\chi_{p_i q_i} r)\eta_p^{\iota'}(\phi)\mathbf{i}_\phi\Big)\Big] \tag{55b}$$

$$\mathbf{g}_i^{\mathrm{TM}} = A_z^{\mathrm{TM}}\Big[\psi_{l_i}(z)\Big(J_p(\chi_{p_i q_i} r)\eta_p^\iota(\phi)\mathbf{i}_z\Big)\Big] \tag{55c}$$

while the terms $\nabla \times \mathbf{f}_i$ and $\nabla \times \mathbf{g}_i$ in (25) write

$$\begin{aligned}\nabla \times \mathbf{f}_i^{\mathrm{TE}} = A_t^{\mathrm{TE}}\Big[&\varphi'_{l_i}(z)\Big(-\tilde{\chi}_{p_i q_i} J'_{p_i}(\tilde{\chi}_{p_i q_i} r)\eta_{p_i}^\iota(\phi)\mathbf{i}_r \\ &-\frac{p_i}{r} J_{p_i}(\tilde{\chi}_{p_i q_i} r)\eta_{p_i}^{\iota'}(\phi)\mathbf{i}_\phi\Big) \\ &+\varphi_{l_i}(z)\Big(-\tilde{\chi}_{p_i q_i}^2 J_{p_i}(\tilde{\chi}_{p_i q_i} r)\eta_{p_i}^\iota(\phi)\Big)\mathbf{i}_z\Big]\end{aligned} \tag{56a}$$

$$\begin{aligned}\nabla \times \mathbf{f}_i^{\mathrm{TM}} = A_t^{\mathrm{TM}}\Big[&\varphi'_{l_i}(z)\Big(-\frac{p_i}{r} J_{p_i}(\chi_{p_i q_i} r)\eta_{p_i}^{\iota'}(\phi)\mathbf{i}_r \\ &+\chi_{p_i q_i} J'_{p_i}(\chi_{p_i q_i} r)\eta_{p_i}^\iota(\phi)\mathbf{i}_\phi\Big)\Big]\end{aligned} \tag{56b}$$

$$\begin{aligned}\nabla \times \mathbf{g}_i^{\mathrm{TM}} = A_z^{\mathrm{TM}}\Big[&\psi_{l_i}(z)\Big(\frac{p_i}{r} J_p(\chi_{p_i q_i} r)\eta_p^{\iota'}(\phi)\mathbf{i}_r \\ &-\chi_{p_i q_i} J'_p(\chi_{p_i q_i} r)\eta_p^\iota(\phi)\mathbf{i}_\phi\Big)\Big]\end{aligned} \tag{56c}$$

APPENDIX C
EXPRESSIONS FOR THE LONGITUDINAL INTEGRALS

Apart from an exchange of indices, six cases for the longitudinal integrals (28) are possible

$$\mathbf{D}_1(i, j, k) = \int_I \varphi_i(z)\varphi_j(z)\varphi_k(z)\mathrm{d}z \tag{57a}$$

$$\mathbf{D}_2(i, j, k) = \int_I \varphi_i(z)\varphi'_j(z)\varphi_k(z)\mathrm{d}z \tag{57b}$$

$$\mathbf{D}_3(i, j, k) = \int_I \varphi'_i(z)\varphi'_j(z)\varphi_k(z)\mathrm{d}z \tag{57c}$$

$$\mathbf{D}_4(i, j, k) = \int_I \varphi_i(z)\psi_j(z)\varphi_k(z)\mathrm{d}z \tag{57d}$$

$$\mathbf{D}_5(i, j, k) = \int_I \varphi'_i(z)\psi_j(z)\varphi_k(z)\mathrm{d}z \tag{57e}$$

$$\mathbf{D}_6(i, j, k) = \int_I \psi_i(z)\psi_j(z)\varphi_k(z)\mathrm{d}z \tag{57f}$$

where the first two terms derive from the FEM discretization and the third term $\varphi_k(z)$ from the expansion (27). The integration domain I requires special attention. Under the hypothesis, here adopted, that the FEM nodes are evenly spaced (basis length equal to a), the basis Lagrange polynomials are equal unless a coordinate translation. Assuming that, after a suitable coordinate translation, $I = [-a/2, a/2]$, the first-degree Lagrange polynomials write

$$\begin{aligned}\psi_1(z) &= -\frac{1}{2}\left(\frac{2}{a}z - 1\right) \\ \psi_2(z) &= \frac{1}{2}\left(\frac{2}{a}z + 1\right)\end{aligned} \tag{58}$$

while the second-degree Lagrange polynomials and their derivatives write

$$\begin{aligned}
\varphi_1(z) &= \frac{z}{a}\left(\frac{2}{a}z - 1\right)\\
\varphi_2(z) &= -\left(\frac{2}{a}z - 1\right)\left(\frac{2}{a}z + 1\right)\\
\varphi_3(z) &= \frac{z}{a}\left(\frac{2}{a}z + 1\right)
\end{aligned} \tag{59}$$

$$\begin{aligned}
\varphi_1'(z) &= \frac{1}{a}\left(\frac{4}{a}z - 1\right)\\
\varphi_2'(z) &= -\frac{8}{a^2}z\\
\varphi_3'(z) &= \frac{1}{a}\left(\frac{4}{a}z + 1\right)
\end{aligned} \tag{60}$$

Then, (57) writes

$$\begin{aligned}
\mathbf{D}_1(i, j, k = 1) &= a\begin{pmatrix} \frac{13}{140} & \frac{1}{21} & -\frac{1}{140}\\ \frac{1}{21} & \frac{4}{105} & -\frac{2}{105}\\ -\frac{1}{140} & -\frac{2}{105} & -\frac{1}{140} \end{pmatrix}\\
\mathbf{D}_1(i, j, k = 2) &= a\begin{pmatrix} \frac{1}{21} & \frac{4}{105} & -\frac{2}{105}\\ \frac{4}{105} & \frac{16}{35} & \frac{4}{105}\\ -\frac{2}{105} & \frac{4}{105} & \frac{1}{21} \end{pmatrix}\\
\mathbf{D}_1(i, j, k = 3) &= a\begin{pmatrix} -\frac{1}{140} & -\frac{2}{105} & -\frac{1}{140}\\ -\frac{2}{105} & \frac{4}{105} & \frac{1}{21}\\ -\frac{1}{140} & \frac{1}{21} & \frac{13}{140} \end{pmatrix}
\end{aligned} \tag{61}$$

$$\begin{aligned}
\mathbf{D}_2(i, j, k = 1) &= \begin{pmatrix} -\frac{1}{3} & \frac{2}{5} & -\frac{1}{15}\\ -\frac{1}{5} & \frac{4}{15} & -\frac{1}{15}\\ \frac{1}{30} & 0 & -\frac{1}{30} \end{pmatrix}\\
\mathbf{D}_2(i, j, k = 2) &= \begin{pmatrix} -\frac{1}{5} & \frac{4}{15} & -\frac{1}{15}\\ -\frac{8}{15} & 0 & \frac{8}{15}\\ \frac{1}{15} & -\frac{4}{15} & \frac{1}{5} \end{pmatrix}\\
\mathbf{D}_2(i, j, k = 3) &= \begin{pmatrix} \frac{1}{30} & 0 & -\frac{1}{30}\\ \frac{1}{15} & -\frac{4}{15} & \frac{1}{5}\\ \frac{1}{15} & -\frac{2}{5} & \frac{1}{3} \end{pmatrix}
\end{aligned} \tag{62}$$

$$\begin{aligned}
\mathbf{D}_3(i, j, k = 1) &= \frac{1}{a}\begin{pmatrix} \frac{37}{30} & -\frac{22}{15} & \frac{7}{30}\\ -\frac{22}{15} & \frac{8}{5} & -\frac{2}{15}\\ \frac{7}{30} & -\frac{2}{15} & -\frac{1}{10} \end{pmatrix}\\
\mathbf{D}_3(i, j, k = 2) &= \frac{1}{a}\begin{pmatrix} \frac{6}{5} & -\frac{16}{15} & -\frac{2}{15}\\ -\frac{16}{15} & \frac{32}{15} & -\frac{16}{15}\\ -\frac{2}{15} & -\frac{16}{15} & \frac{6}{5} \end{pmatrix}\\
\mathbf{D}_3(i, j, k = 3) &= \frac{1}{a}\begin{pmatrix} -\frac{1}{10} & -\frac{2}{15} & \frac{7}{30}\\ -\frac{2}{15} & \frac{8}{5} & -\frac{22}{15}\\ \frac{7}{30} & -\frac{22}{15} & \frac{37}{30} \end{pmatrix}
\end{aligned} \tag{63}$$

$$\begin{aligned}
\mathbf{D}_4(i, j, k = 1) &= a\begin{pmatrix} \frac{7}{60} & \frac{1}{60}\\ \frac{1}{15} & 0\\ -\frac{1}{60} & -\frac{1}{60} \end{pmatrix}\\
\mathbf{D}_4(i, j, k = 2) &= a\begin{pmatrix} \frac{1}{15} & 0\\ \frac{4}{15} & \frac{4}{15}\\ 0 & \frac{1}{15} \end{pmatrix}\\
\mathbf{D}_4(i, j, k = 3) &= a\begin{pmatrix} -\frac{1}{60} & -\frac{1}{60}\\ 0 & \frac{1}{15}\\ \frac{1}{60} & \frac{7}{60} \end{pmatrix}
\end{aligned} \tag{64}$$

$$\begin{aligned}
\mathbf{D}_5(i, j, k = 1) &= \begin{pmatrix} -\frac{13}{30} & -\frac{1}{15}\\ \frac{8}{15} & \frac{2}{15}\\ -\frac{1}{10} & -\frac{1}{15} \end{pmatrix}\\
\mathbf{D}_5(i, j, k = 2) &= \begin{pmatrix} -\frac{7}{15} & -\frac{1}{5}\\ \frac{4}{15} & -\frac{4}{15}\\ \frac{1}{5} & \frac{7}{15} \end{pmatrix}\\
\mathbf{D}_5(i, j, k = 3) &= \begin{pmatrix} \frac{1}{15} & \frac{1}{10}\\ -\frac{2}{15} & -\frac{8}{15}\\ \frac{1}{15} & \frac{13}{30} \end{pmatrix}
\end{aligned} \tag{65}$$

$$\begin{aligned}
\mathbf{D}_6(i, j, k = 1) &= a\begin{pmatrix} \frac{3}{20} & \frac{1}{60}\\ \frac{1}{60} & -\frac{1}{60} \end{pmatrix}\\
\mathbf{D}_6(i, j, k = 2) &= a\begin{pmatrix} \frac{1}{5} & \frac{2}{15}\\ \frac{2}{15} & \frac{1}{5} \end{pmatrix}\\
\mathbf{D}_6(i, j, k = 3) &= a\begin{pmatrix} -\frac{1}{60} & \frac{1}{60}\\ \frac{1}{60} & \frac{3}{20} \end{pmatrix}
\end{aligned} \tag{66}$$

Apart from the constant a, the expressions (61)–(66) can be stored in memory and retrieved when necessary.

REFERENCES

[1] M. K. Thumm and W. Kasparek, "Passive high-power microwave components," *IEEE Plasma Sci.*, vol. 30, no. 3, pp. 755–786, Jun. 2002.

[2] O. A. Peverini, M. Lumia, G. Addamo, G. Virone, and N. J. G. Fonseca, "How 3D-printing is changing RF front-end design for space applications," *IEEE J. Microwaves*, vol. 3, no. 2, pp. 800–814, Apr. 2023.

[3] T. P. Wangler, *RF Linear Accelerators*. Hoboken, NJ, USA: Wiley, 2008.

[4] P. Booth and E. V. Lluch, "Enhancing the performance of waveguide filters using additive manufacturing," *Proc. IEEE*, vol. 105, no. 4, pp. 613–619, Apr. 2017.

[5] W. Huting and K. Webb, "Comparison of mode-matching and differential equation techniques in the analysis of waveguide transitions," *IEEE Trans. Microw. Theory Techn.*, vol. 39, no. 2, pp. 280–286, Feb. 1991.

[6] D. S. Nagarkoti, R. Sharma, R. L. Dua, and P. K. Jain, "Analysis of nonlinear cylindrical waveguide taper using modal matching technique," *WARSE Int. J. Microw. Appl.*, vol. 1, no. 1, pp. 5–12, 2012.

[7] F. Sporleder and H. G. Unger, "Waveguide tapers, transitions, and couplers," *P. Peregrinus*, ser. IEEE Electromagnetic Waves, 1979.

[8] B. Z. Katsenelenbaum, L. Mercader del Rio, M. Pereyaslavets, M. Sorolla Ayza, and M. Thumm, *Theory of Nonuniform Waveguides: The Cross-Section Method*. London, U.K.: IET, 1998.

[9] I. Arnedo, I. Arregui, A. Lujambio, M. Chudzik, M. A. G. Laso, and T. Lopetegi, "Synthesis of microwave filters by inverse scattering using a closed-form expression valid for rational frequency responses," *IEEE Trans. Microw. Theory Techn.*, vol. 60, no. 5, pp. 1244–1257, May 2012.

[10] I. Arnedo et al., “Direct and exact synthesis: Controlling the microwaves by means of synthesized passive components with smooth profiles,” *IEEE Microw. Mag.*, vol. 16, no. 4, pp. 114–128, May 2015.

[11] M. Guglielmi, R. Sorrentino, and G. Conciauro, *Advanced Modal Analysis: CAD Techniques for Waveguide Components and Filter*. Hoboken, NJ, USA: Wiley, 1999.

[12] M. Guglielmi, G. Gheri, M. Calamia, and G. Pelosi, “Rigorous multimode network numerical representation of inductive step,” *IEEE Trans. Microw. Theory Techn.*, vol. 42, no. 2, pp. 317–326, Feb. 1994.

[13] I. Stevanovic, P. Crespo-Valero, and J. R. Mosig, “An integral-equation technique for solving thick irises in rectangular waveguides,” *IEEE Trans. Microw. Theory Techn.*, vol. 54, no. 1, pp. 189–197, Jan. 2006.

[14] G. Conciauro, P. Arcioni, M. Bressan, and L. Perregrini, “Wideband modeling of arbitrarily shaped H-plane waveguide components by the ‘boundary integral-resonant mode expansion method’,” *IEEE Trans. Microw. Theory Techn.*, vol. 44, no. 7, pp. 1057–1066, Jul. 1996.

[15] G. Pelosi, R. Coccioli, and S. Selleri, *Quick Finite Elements for Electromagnetic Waves*, 2nd ed. Norwood, MA, USA: Artech House, 2009.

[16] Dassault Systémes, “CST studio suite,” 2023. [Online]. Available: https://www.3ds.com/products-services/simulia/products/cst-studio-suite/

[17] G. G. Gentili, L. Accatino, and G. Bertin, “The generalized 2.5-D finite-element method for analysis of waveguide components,” *IEEE Trans. Microw. Theory Techn.*, vol. 64, no. 8, pp. 2392–2400, Aug. 2016.

[18] G. Garcia-Contreras et al., “Advanced modeling of rectangular waveguide devices with smooth profiles by hierarchical model reduction,” *IEEE Trans. Microw. Theory Techn.*, vol. 71, no. 11, pp. 4692–4702, Nov. 2023.

[19] D. H. Kwon and D. H. Werner, “Transformation electromagnetics: An overview of the theory and applications,” *IEEE Antennas Propag. Mag.*, vol. 52, no. 1, pp. 24–46, Feb. 2010.

[20] W. X. Jiang, W. X. Tang, and T.-J. Cui, “Transformation optics and applications in microwave frequencies,” *Prog. Electromagnetics Res.*, vol. 149, pp. 251–273, 2014.

[21] M. McCall et al., “Roadmap on transformation optics,” *J. Opt.*, vol. 20, no. 6, 2018, Art. no. 063001.

[22] T. N. Kaifas, E. Vafiadis, X. M. Mitsalas, G. Granet, J. N. Sahalos, and G. A. Kyriakou, “Transformation electromagnetics eigenanalysis of perfect electric conductor cavities,” *IET Microw., Antennas Propag.*, vol. 12, no. 8, pp. 1435–1443, 2018.

[23] O. Ozgun and M. Kuzuoglu, “Transformation electromagnetics based analysis of waveguides with random rough or periodic grooved surfaces,” *IEEE Trans. Microw. Theory Techn.*, vol. 61, no. 2, pp. 709–719, Feb. 2013.

[24] G. Gentili, G. Giannetti, M. Khosronejad, G. Pelosi, and S. Selleri, “Modes computation in arbitrarily shaped waveguides by a transformation optics approach,” *Int. J. RF Microw. Comput.-Aided Eng.*, vol. 31, no. 1, 2021, Art. no. e22480.

[25] G. G. Gentili, G. Giannetti, G. Pelosi, and S. Selleri, “Considerations on boundary conditions in transformation optics for complete field computation in generic waveguides,” *Microw. Opt. Technol. Lett.*, vol. 65, no. 1, pp. 373–380, 2023.

[26] G. G. Gentili, G. Giannetti, G. Pelosi, and S. Selleri, “Transformation optics combined with line-integrals for fast and efficient mode matching analysis of waveguide devices,” *IEEE J. Microwaves*, vol. 3, no. 3, pp. 1051–1060, Jul. 2023.

[27] G. Bertin, B. Piovano, L. Accatino, and M. Mongiardo, “Full-wave design and optimization of circular waveguide polarizers with elliptical irises,” *IEEE Trans. Microw. Theory Techn.*, vol. 50, no. 4, pp. 1077–1083, Apr. 2002.

[28] G. Virone, R. Tascone, O. A. Peverini, and R. Orta, “Optimum-iris-set concept for waveguide polarizers,” *IEEE Microw. Wireless Compon. Lett.*, vol. 17, no. 3, pp. 202–204, Mar. 2007.

[29] G. Olivier, J. Thermeau, P. Bosland, and C. Darve, “ESS cryomodules for elliptical cavities,” in *Proc. 16th Int. Conf. RF Supercond.*, 2013, pp. 341–344.

[30] P. Arcioni, M. Bressan, and L. Perregrini, “A new boundary integral approach to the determination of the resonant modes of arbitrarily shaped cavities,” *IEEE Trans. Microw. Theory Techn.*, vol. 43, no. 8, pp. 1848–1856, Aug. 1995.

[31] T. Stange, “Simple broadband circular polarizer in oversized waveguide,” *J. Infrared, Millimeter, THz Waves*, vol. 37, no. 2, pp. 137–146, 2016.

[32] H. Y. Yu, J. Yu, X. Liu, Y. Yao, and X. Chen, “A wideband circularly polarized horn antenna with a tapered elliptical waveguide polarizer,” *IEEE Trans. Antennas Propag.*, vol. 67, no. 6, pp. 3695–3703, Jun. 2019.

[33] C. Tomassoni, O. A. Peverini, G. Venanzoni, G. Addamo, F. Paonessa, and G. Virone, “3D printing of microwave and millimeter-wave filters: Additive manufacturing technologies applied in the development of high-performance filters with novel topologies,” *IEEE Microw. Mag.*, vol. 21, no. 6, pp. 24–45, Jun. 2020.

[34] A. T. Villeneuve, “Orthogonality relationships for waveguides and cavities with inhomogeneous anisotropic media,” *IRE Trans. Microw. Theory Techn.*, vol. 7, no. 4, pp. 441–446, 1959.

[35] M. S. Gockenbach, *Understanding and Implementing the Finite Element Method* (ser. Other Titles in Applied Mathematics). Philadelphia, PA, USA: SIAM, 2006.

[36] R. E. Collin, *Field Theory of Guided Waves, Ser. IEEE Press Series on Electromagnetic Wave Theory*. Hoboken, NJ, USA: Wiley, 1990.

[37] M. L. Crawford, “Generation of standard EM fields using TEM transmission cells,” *IEEE Trans. Electromagn. Compat.*, vol. EMC-16, no. 4, pp. 189–195, Nov. 1974.

[38] C. Spindelberger, G. Giannetti, and H. Arthaber, “Increasing the test-volume of open TEM cells by using an asymmetric design,” in *Proc. IEEE Kleinheubach Conf.*, 2022, pp. 1–4.

[39] G. Giannetti, C. Spindelberger, and H. Arthaber, “Simple semianalytical septum design for improved matching in open TEM cells,” *IEEE Lett. Electromagn. Compat. Pract. Appl.*, vol. 6, no. 1, pp. 6–10, Mar. 2024.

GIACOMO GIANNETTI (Graduate Student Member, IEEE) received the B.Sc. degree (*cum laude*) in electronic and telecommunications engineering from the University of Florence, Florence, Italy, in 2019, and the M.Sc. degree (*cum laude*) in electronic engineering from the Sapienza University of Rome, Rome, Italy, in 2021, with the award as an excellent graduate. He is currently working toward the Ph.D. degree in electromagnetism with the University of Florence. He was a Student with the Technical University of Vienna, Vienna, Austria, and the National Laboratory of Frascati, Frascati, Italy, and a Research Guest with Kiel University, Kiel, Germany. He was awarded the EuMA Internship Award with the University of Birmingham, Birmingham, United Kingdom, as a host institution. His research interests include microwave devices and computational electromagnetics.

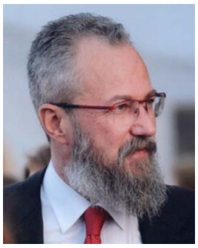

STEFANO SELLERI (Senior Member, IEEE) was born in Viareggio, Italy, in 1968. He received the Laurea degree (*cum laude*) in electronic engineering and the Ph.D. degree in computer science and telecommunications from the University of Florence, Florence, Italy, in 1992 and 1997, respectively. He is currently an Associate Professor with the University of Florence. He has authored or coauthored more than 120 papers in international referred journals and eight books or book chapters. He conducts research on the numerical modeling of microwave, devices, and circuits with particular attention to numerical optimization with the University of Florence. He is on the editorial board of IEEE TRANSACTIONS ON ANTENNAS AND PROPAGATION and *The Applied Computational Electromagnetics Society*.

GIAN GUIDO GENTILI received the Laurea degree in electronics engineering from the Politecnico di Milano, Milan, Italy, in 1987. He was a Researcher with the Dipartimento di Elettronica ed Informazione, National Research Council (CNR), Center for Space Telecommunications, Politecnico di Milano, in 1989. In 2001, he was a Senior CNR Researcher. He was an Associate Professor with the Politecnico di Milano, in 2002. He was a Visiting Scholar with Politecnica de Madrid in 1993 and 1995, respectively. He is responsible for the Electromagnetics Laboratory of Politecnico di Milano “Wavelab.” His research interests include numerical method for electromagnetics (finite elements, method of moments, and mode-matching), antennas and feed systems for terrestrial and space applications, microwave passive devices and filters, plasmonics. He organized the Italian National Conference on Appled Electromagnetics, RiNem 2000, Como, Italy.

GINES GARCIA-CONTRERAS was born in Madrid, Spain, in 1997. He received the B.Sc. and M.Sc. degrees in electrical engineering in 2019 and 2021, respectively, from the Universidad Autónoma de Madrid (UAM), Madrid, Spain, where he is currently working toward the Ph.D. degree in applied electromagnetics with the "Radiofrecuencia: Circuitos, Antenas y Sistemas" Research Group. From April 2022 to June 2022, he was a Visiting Scholar with the Politecnico di Milan, Milan, Italy. His research interests include numerical and hybrid methods for electromagnetic simulation, symmetries, and periodic structures.

JUAN CÓRCOLES (Senior Member, IEEE) was born in Albacete, Spain, in 1981. He received the B.Sc. and M.Sc. degrees in electrical engineering (Ingeniero de Telecomunicacion degree) and the Ph.D. degree from the Universidad Politecnico de Madrid, Madrid, Spain, in 2004 and 2009, respectively. From 2010 to 2023, he was with the Universidad Autónoma de Madrid, Madrid, where he became an Associate Professor in 2015. Since 2023, he has been with Universidad Politecnico de Madrid. His research interests include applied and computational electromagnetics, particularly in the development of numerical methods and optimization techniques for the analysis and design of microwave circuits, antennas, and other related applications.

JORGE A. RUIZ-CRUZ (Senior Member, IEEE) received the Ingeniero de Telecomunicacion and Ph.D. degrees from the Universidad Politecnica de Madrid (UPM), Madrid, Spain, in 1999 and 2005, respectively. In 2000, he was with the company RYMSA, Mexico. He was a Research Associate with the University of Maryland, College Park, MD, USA. In 2006, he joined Universidad Autonoma de Madrid, Madrid where he became an Associate Professor in 2009, and Full Professor in 2021. In 2023 he was with UPM, as a Full Professor with the Department of Signals, Systems and Radiocommunications. His research interests include computer-aided design of microwave passive devices and systems,filters, multiplexers, orthomodes, and many more.

Open Access provided by 'Università degli Studi di Firenze' within the CRUI CARE Agreement